

# Enhanced Thermodynamic, Pharmacokinetic and Theranostic Properties of Polymeric Micelles via Hydrophobic Core-clustering of Superparamagnetic Iron Oxide Nanoparticles

**Yixin Jiang**

Inha Medical College: Inha University School of Medicine

**Junghan Lee**

Inha Medical College: Inha University School of Medicine

**Hye-Min Park**

Inha Medical College: Inha University School of Medicine

**Kyung-Ju Shin**

Inha Medical College: Inha University School of Medicine

**Su-Geun Yang** (✉ [orosyang@gmail.com](mailto:orosyang@gmail.com))

Inha University College of Medicine <https://orcid.org/0000-0001-5278-8723>

---

## Research Article

**Keywords:** polymeric micelles, superparamagnetic iron oxide, critical micelle concentration, theranostic nanoparticle, micelle stability, SPIO clustering

**Posted Date:** November 8th, 2021

**DOI:** <https://doi.org/10.21203/rs.3.rs-1037864/v1>

**License:**  This work is licensed under a Creative Commons Attribution 4.0 International License.

[Read Full License](#)

---

**Version of Record:** A version of this preprint was published at Biomaterials Research on March 7th, 2022. See the published version at <https://doi.org/10.1186/s40824-022-00255-9>.

# Abstract

**Background:** Superparamagnetic iron oxide nanoparticles (SPIO) have been applied for decades to design theranostic polymeric micelles for targeted cancer therapy and diagnostic MR imaging. However, the effects of SPIO on the physicochemical, and biological properties of polymeric micelles have not yet been fully elucidated. Therefore, we investigated potential effect of SPIO on the physical and biological properties of theranostic polymeric micelles using representative cancer drug (doxorubicin; Doxo) and polymer carrier (i.e., poly (ethylene glycol)-co-poly(D,L-lactide), PEG-PLA).

**Methods:** SPIO were synthesized from  $\text{Fe}(\text{acetyl acetonate})_3$  in an aryl ether. SPIO and Doxo were loaded into the polymeric micelles by a solvent-evaporation method. We observed the effect of SPIO-clustering on drug loading, micelle size, thermodynamic stability, and theranostic property of PEG-PLA polymeric micelles. In addition, cellular uptake behaviors, pharmacokinetic and biodistribution study were performed.

**Results:** SPIO formed hydrophobic geometric cavity in the micelle core and significantly affected the integrity of micelles in terms of micelle size, Doxo loading, critical micelle concentration (CMC) and in vitro dissociation. In vivo pharmacokinetic studies also showed the enhanced Area Under Curve (AUC) and elongated the half-life of Doxo.

**Conclusions:** Clustered SPIO in micelles largely affects not only MR imaging properties but also biological and physical properties of polymeric micelles.

## Background

Multifunctional nanomedicine that integrates diagnostic and therapeutic functions has received considerable attention as the next generation of medicine [1–9]. Unlike traditional small molecular contrast agents or drugs, multifunctional nanomedicine has the potential to provide molecular diagnosis, targeted therapy, and simultaneous treatment and monitoring of therapeutic efficacy in one system [3, 10–13]. The ideal theranostic nanomedicine should provide high drug loading densities, drug-carrier biocompatibility, responsive release mechanism to improve drug delivery efficiency, and imaging sensitivity to pre-validate and monitor therapy [14]. One of the major challenges for the development of nanomedicine is the incorporation of multiple functional components (e.g. therapeutic drugs, imaging agents, and polymer carriers) into one nanocomposite system within a small size confinement (e.g., <100 nm). Despite the explosive development of many multifunctional nanomedicine platforms, the interactions between each component and the influence of one component over the performance of the others have not been systematically investigated. Understanding of the material interactions at the nanoscale is critically important for the successful development and implementation of theranostic nanomaterials in medicine.

For decades, theranostic polymeric micelles have been studied for cancer molecular imaging and targeted drug delivery applications [8, 15, 16]. An anticancer drug, doxorubicin (Doxo) and an imaging

agent, superparamagnetic iron oxide nanoparticles (SPIO) were co-loaded inside the micelle core (Fig. 1A) and the micelle surface was further functionalized with a peptide that targets cell surface markers over-expressed in the tumor vasculature. Previous studies showed that clustering of hydrophobic SPIO in the hydrophobic micelle core resulted in dramatically increased  $T_2$  relaxivity, which allowed for the subsequent cancer-specific imaging of  $\alpha_v\beta_3$  integrins in solid tumors in vivo by magnetic resonance imaging (MRI) [1, 17–21]. In this paper, we studied the dynamics of interactions between the imaging agent (i.e., SPIO), small molecular drug (i.e., Doxo) and polymer carrier (i.e., poly (ethylene glycol)-co-poly(D, L-lactide), PEG-PLA). These results indicated that SPIO encapsulation significantly increased the loading density of Doxo inside polymeric micelles and prolonged the blood circulation time of the Doxo-loaded micelles. The improved properties correlated well with increased thermodynamic as well as kinetic stabilities of SPIO-loaded micelles in aqueous solution over SPIO-free micelles. It provided the physico-chemical insights and structure-property relationships for the further optimization of multifunctional micellar nanomedicine.

## Methods

## Materials

Poly(ethylene glycol)-poly(D,L-lactide) (PEG-PLA, PEG and PLA M.W.=5 kD) was synthesized following the reported method [22]. The molecular weight and polydispersity of PEG-PLA were also characterized by gel permeation chromatography and  $^1\text{H-NMR}$ . Doxorubicin-HCl for injection (2 mg/ml) was purchased from Bedford Laboratories (Adriamycin<sup>®</sup>, Bedford, OH), and treated with triethylamine to obtain the hydrophobic Doxo. Phenyl ether (99%), benzyl ether (99%), 1,2-hexadecanediol (97%), oleic acid (99%), oleylamine (>70%), tetrahydrofuran (THF), hexane, dimethyl sulfoxide (DMSO), and iron(III) acetylacetonate were purchased from Sigma-Aldrich Chemical Co. (Saint Louis, MO). 1,2-Distearoyl-sn-glycero-3-phosphoethanolamine-N-[methoxy (polyethylene glycol)-5000] (ammonium salt) (DSPE-PEG) was purchased from Avanti Polar Lipids, Inc. (Alabaster, AL). All organic solvents are of analytical grade.

## Preparation of Doxo-SPIO-micelles

Doxo-SPIO-micelles were fabricated according to the published procedure [18, 23]. In brief, highly crystalline and monodisperse SPIO were synthesized from  $\text{Fe}(\text{acetyl acetonate})_3$  in an aryl ether [23]. For the micelles, PEG-PLA was used as surfactant molecules for the encapsulation of SPIO and Doxo. Subsequently, SPIO with 7 nm diameter and Doxo were loaded into the polymeric micelles by a solvent-evaporation method [18]. SPIO and Doxo were dissolved in 800  $\mu\text{l}$  of THF and 200  $\mu\text{l}$  of DMSO. Then, THF and DMSO were mixed together, and this mixture was added into water (3 ml) under sonication (LH700S, ULSSO HITECH Co.). After the sonication, the solution was shaken overnight to allow the organic solvent to evaporate. Finally, Doxo-SPIO-micelles were purified by Millipore centrifuge filtration (MW cut off: 30kD). The weight ratios (mg) of PEG-PLA:SPIO:Doxo were varied over three values: 10:2.5:2; 10:5:2; and 10:10:2.

## Characterization of Doxo-SPIO-micelles

## Hydrodynamic diameter

The hydrodynamic diameter ( $D_H$ ) of the Doxo-SPIO-micelles was estimated by dynamic light scattering method (DLS, Nano-ZS90, Malvern Panalytical Co. United Kingdom). Doxo-SPIO-micelles, made with different ratios of PEG-PLA:SPIO:Doxo (10:10:2, 10:5:2, 10:2.5:2), were introduced to DLS.

## Transmission electron microscopy (TEM) imaging

To confirm the size and morphology of Doxo-SPIO-micelles, transmission electron microscopy (TEM) images for nanoparticles were obtained using an FE-TEM (JEM 2100F, JEOL Co. Japan). For Doxo-SPIO-micelles, formvar coated-copper grids were glow discharged using a vacuum coating unit. Each sample solution was dropped on to the glow discharged grid. After 2 minutes of standing, the excess solution was removed by blotting the grid against a filter paper. Negative staining (dark field) of sample was done by additional dropping of 2% phosphotungstic acid (PTA) solution to the grid. For SPIO, TEM samples were prepared by allowing a small drop of SPIO suspension in hexane to dry on carbon-coated copper grids without negative staining. All TEM images were obtained at an accelerating voltage of 120 kV.

## Determination of drug loading content (DLC)

The DLC of the micelle was determined by UV-VIS analysis. At first, micelle solutions were frozen and lyophilized to yield the solid micelle samples. Then the dried samples were weighed and re-dissolved in a mixture of chloroform and DMSO (1:1, v/v) under bath-sonication for 30 minutes. The suspending SPIO were centrifuged down, and upper layer of solution was transferred to UV-VIS spectrometer (Spectra Max Plus 384 Microplate Reader, Molecular Devices, USA). The absorbance at 480 nm was measured to determine the Doxo content in the solution with a previously established calibration curve. The weight % of Doxo, entrapped in the core of micelle, was calculated from the dried weight of Doxo-SPIO-micelles and the amount of Doxo incorporated.

## Estimation of thermodynamic properties of Doxo-SPIO-micelles

## Critical micelle concentration (CMC) determination

The CMC of the polymer was estimated to investigate the effect of SPIO on the micelle stability. Following the reported method, a solution of pyrene in dichloromethane was dried by a stream of nitrogen [24]. An aqueous solution of micelles was subsequently added to the dried film followed by gentle shaking for 72 h at 37°C. The final concentration of pyrene was  $1.0 \times 10^{-8} \text{ mol}\cdot\text{L}^{-1}$  while that of PEG-PLA was varied from 0.1 to 100  $\mu\text{g}\cdot\text{mL}^{-1}$ . The CMC was calculated by plotting the fluorescence intensity of pyrene ( $\lambda_{em} = 390 \text{ nm}$ ,  $\lambda_{ex} = 333 \text{ nm}$ ) as a function of PEG-PLA concentration.

## Evaluation of dissociation kinetics of Doxo-SPIO-micelles

A dissociation of micelles at a concentration below the CMC ( $100 \mu\text{g}\cdot\text{mL}^{-1}$  and  $8 \mu\text{g}\cdot\text{mL}^{-1}$ , respectively) was also evaluated. SPIO-loaded micelles and SPIO-free micelles encapsulating pyrene were prepared in HEPES buffer pH 7.4 at the polymer concentration of  $1.5 \text{ mg}\cdot\text{mL}^{-1}$  according to the previously reported method. After micelle formation, the micelle solution was diluted, and the fluorescent intensity ( $\lambda_{\text{ex}} = 333$ ,  $\lambda_{\text{em}} = 390$ ) was recorded at  $37^\circ\text{C}$  over time.

## Estimation of thermodynamic fluidity of micelle core

In this study, we uploaded 1,3-di(1,1'-pyrenyl) propane (DPP) dye in the micelle core and estimated the molecular state of DPP (i.e., excimer formation) to examine the microenvironmental fluidity of the micelle core. DPP was dissolved in chloroform, dried, and reconstituted with ethyl acetate. Then DPP was mixed with the SPIO-loaded or SPIO-free micelles for 72 hrs under  $\text{N}_2$  gas. The final concentration of DPP was  $1.8 \times 10^{-7} \text{ M}$ , while the polymer concentration was  $100 \mu\text{g}\cdot\text{mL}^{-1}$ , above the CMC. The emission intensity of DPP excimer at 478 nm ( $I_{\text{e}}$ ) and monomer at 377 nm ( $I_{\text{m}}$ ) was measured as a function of temperature ( $\lambda_{\text{ex}} = 333 \text{ nm}$ ).

## In vitro drug release study

Doxo-SPIO-micelles were transferred into dialysis tubes (MW cut-off: 50,000 Da, Spectrum Laboratories, USA). The tubes were immersed in 25 ml PBS (pH 7.4) or acetate buffered saline (pH 5.0) solutions. The release of Doxo from micelles was tested under mechanical shaking (100 rpm/min) at  $37^\circ\text{C}$ . At selected time intervals, buffered solution outside the dialysis bag was removed to estimate the released amount of Doxo and replaced with fresh buffer solution. Doxo concentration was calculated based on the fluorescence intensity (ex; 470 nm, em; 590 nm) with a previously established calibration curve. The error bars were obtained from triplicate samples.

## Estimation of MR imaging properties of Doxo-SPIO-micelles

## Estimation of magnetization properties of Doxo-SPIO-micelles

To help understand the MR properties, we measured the magnetization of Doxo-SPIO-micelles. Samples were prepared by pipetting  $5 \mu\text{L}$  of solution containing Doxo-SPIO-loaded micelles into a glass cell ( $4.0 \times 4.0 \times 0.4 \text{ mm}$ ) and attached to the probe with a small amount of silicon grease. Magnetization measurements were conducted using an alternating gradient magnetometer (AGM, Princeton Measurements) at room temperature and up to 1.4 T.

## Estimation of $T_2$ relaxivity of Doxo-SPIO-micelles

MR sensitivity of Doxo-SPIO-micelles was measured at 0.55 T (23.4 MHz) on a Resonance Maran Ultra scanner at  $37^\circ\text{C}$  (Oxford instruments, UK).  $T_2$  relaxation rates ( $1/T_2, \text{ s}^{-1}$ ) were measured using a CPMG

(Carr Purcell Meiboom Gill) pulse sequence.  $T_1$  relaxation rates ( $1/T_1, s^{-1}$ ) were measured using the INVREC pulse sequence with  $TE=5 \times T_1$ . Linear regression analysis of  $1/T_1$  vs total iron concentration yielded the  $T_{1,2}$  relaxivity ( $r_{1,2}$ ).

## Phantom MR imaging of Doxo-SPIO-micelles

To evaluate the clustering effect of SPIO in the micelle on MR sensitivity, we measured  $T_2$  relaxation rates ( $1/T_2, s^{-1}$ ) using a spin echo pulse sequence with  $TR = 6$  s and  $TE$  varied from 9 ms to 150 ms ( $n = 8$ ) on a 4.7 T Varian INOVA scanner. Linear regression analysis of  $1/T_2$  vs. total metal concentration yielded the  $T_2$  relaxivity ( $r_2$ ).

## Cellular uptake behaviors of Doxo-SPIO-micelles

Cellular uptake of different formula of Doxo-SPIO-loaded micelle was evaluated through flow cytometry analysis using H1299 non-small cell lung carcinoma cells. H1299 cells were seeded in 6-well plates (300,000 cells/well) in 2 ml DMEM with 10% FBS and incubated for 24 hrs, followed by co-incubation with Doxo-SPIO-loaded micelles at the Doxo concentration of 10  $\mu\text{g/ml}$  for 2hrs. After the treatment, the cells were washed three times with PBS.

## In vivo pharmacokinetic and biodistribution study

The enhanced thermodynamic stability of micelles through incorporation of SPIO was clearly distinguished from above experiments. In vivo pharmacokinetic stability of Doxo-SPIO-micelles was also identified in our experiment. Doxo-SPIO-micelles, Doxo-micelles and free Doxo were injected via a lateral tail vein into 20–22 g of BALB-C mice at a normalized dose ( $2.5 \text{ mg} \cdot \text{kg}^{-1}$  as Doxo). 50  $\mu\text{L}$  of blood was collected from the retroorbital plexus and immediately centrifuged at 2000 g for 2 min. Doxo concentration in plasma was measured using a microplate fluorescence reader (Spectra Max M5, Molecular devices, CA) after organic solvent extraction [25].

For the body distribution study, each organ was collected and washed with the PBS after sacrificing of mice treated with Doxo-SPIO-micelles, Doxo-micelles, and Doxo (control). For quantification of Doxo content in the kidneys, liver, lungs, spleen, muscle and heart after the injection, mice were euthanized for imaging. Organs were collected, washed with PBS. Organs collected from 3 of Doxo treated mice served as control. Fluorescence image was performed and analyzed with in vivo imaging system (FOBI, NeoScience Co. Republic of Korea).

## Statistical analysis

Quantitative data were presented as the mean  $\pm$  standard deviation and comparisons were carried out using t-text analysis. Statistical significances were described at (\* $P < 0.1$ , \*\* $P < 0.05$ , \*\*\* $p < 0.01$ ).

## Results

### Clustering of SPIO in the micelle core

# Effect of SPIO loading on hydrodynamic size of micelle

For the study, we systematically increased the weight ratio of SPIO while keeping the polymer to drug ratio the same. Fig. 1B shows that the hydrodynamic diameter ( $D_H$ ) of the micelles increased with an increase of SPIO weight ratio. The SPIO-free empty micelles showed  $24 \pm 3$  nm of diameter. The diameter increased to  $80 \pm 13$ ,  $100 \pm 9$  and  $108 \pm 8$  nm, respectively, when SPIO were loaded in the micelles by weight ratio of 15, 30, and 50 % (Fig. 1B). The same results were observed on TEM image analysis. Fig. 1C-F shows that micelle diameter increased by loading amount of SPIO. This observation proves that clustering of SPIO in the micelle core affects the size of micelle.

## Clustering number of SPIO

The clustering number of SPIO in the micelle core was analyzed. Fig. S1 shows the relationship between individual clustering number of SPIO ( $N_{ind}$ ) and the resulting size of Doxo-SPIO-micelles. As demonstrated in Fig. 1 and Fig. S1 clearly shows that the size of the micelles increases in proportion to the clustering number of SPIO.

## The effect of SPIO clustering on thermodynamic stability of Doxo-SPIO-micelles

## The effect of SPIO clustering on CMC of micelle

The estimated the critical micelle concentration (CMC) of SPIO-loaded micelles and SPIO-free micelles were  $11.7 \mu\text{g}\cdot\text{mL}^{-1}$  and  $24.9 \mu\text{g}\cdot\text{mL}^{-1}$ , respectively (Fig. 2A). The micellization energy was calculated from the observed CMC by

$$\Delta G_o = RT \ln X_{cmc} \quad (\text{eq. 1})$$

where  $R$  = gas constant ( $8.3143 \text{ J/K}\cdot\text{mole}$ ),  $T$  = temperature ( $^\circ\text{K}$ ),  $X_{cmc}$  = concentration at CMC in molar fraction, and  $G_o$  = micellization energy ( $\text{kJ}\cdot\text{mole}^{-1}$ ) [26]. The micellization energy of SPIO-loaded micelles and SPIO-free micelles were  $29.3 \pm 0.14 \text{ kJ/mole}$  and  $-27.3 \pm 0.11 \text{ kJ}\cdot\text{mole}^{-1}$ , respectively.

## Effect of SPIO clustering on the dissociation of micelle

The concentration of SPIO-free micelles ( $24.9 \mu\text{g/ml}$ ) at the turning point extrapolated from the graph matches. Interestingly, SPIO-micelles were displayed the well-accepted CMC value at  $11.7 \mu\text{g/ml}$  (Fig. 2A).

As shown in Fig. 2B, the initial fluorescence intensity of both micelles decreased gradually. The rate constant of dissociation for SPIO-free micelles was estimated as  $0.55 \pm 0.11 \text{ min}^{-1}$  at  $37^\circ\text{C}$ . On the other hand, the dissociation rate constant for SPIO-loaded micelles was  $0.26 \pm 0.03 \text{ min}^{-1}$  at the same temperature.

## Effect of SPIO clustering on Doxo loading and release

# Effect of SPIO clustering on the Doxo loading

Incorporation of SPIO significantly increased the drug loading content (DLC) of Doxo, which was measured as the weight percentage of Doxo over the total weight of Doxo-SPIO-micelles. In SPIO-free micelles, the DLC was  $3.3 \pm 2.0\%$ ; while the DLC increased to  $12.4\%$  ( $p < 0.001$ ,  $n = 4$  when SPIO (15% wt) was co-encapsulated inside the micelles (Fig. 3A). Moreover, the encapsulation of SPIO also helped improve the drug loading efficiency (DLE), which was calculated as the weight percentage of encapsulated Doxo over the initial amount of drug. The SPIO-loaded micelles showed much higher DLE (90.9%) than the SPIO-free micelles ( $19.8 \pm 2.0\%$ ,  $p < 0.001$ ,  $n = 4$ , Fig. 3B).

## Mechanism of increased drug loading on Doxo-SPIO-micelles

To elucidate the mechanism of increased drug loading, we used 1,3-(1,1'-dipyrenyl)-propane (DPP) dye to probe the microenvironment of micelle core. In this series of experiments, we immersed the SPIO-loaded or SPIO-free PEG-PLA micelles (we excluded Doxo from these micelles to avoid its fluorescence interference) in the DPP solution at  $1.8 \cdot 10^{-7}$  M for 72 hrs under  $N_2$ . The PEG-PLA concentrations were controlled at  $100 \mu\text{g}\cdot\text{mL}^{-1}$ , well above CMC for each formulation (see CMC values below). The ratio of emission intensity of DPP excimer at 478 nm ( $I_e$ ) and monomer at 377 nm ( $I_m$ ) at an excitation wavelength of 333 nm was measured as a function of temperature (Fig. 4). Fig. 4A and 4C show SPIO-loaded micelles exert higher  $I_e/I_m$  values than those of SPIO-free micelles at all range of temperatures. More specifically, the  $I_e/I_m$  value of SPIO-free micelles at  $37^\circ\text{C}$  was 0.07 compared to 0.19 for SPIO-loaded micelles. Generally, excimer formation is limited in a highly viscous environment, leading to relatively higher intensity of monomer ( $I_m$ ) and lower value of  $I_e/I_m$ . Interestingly, micelles show a biphasic behavior with an inflection temperature at  $37.3^\circ\text{C}$  (Fig. 4B), compared to  $45.1^\circ\text{C}$  of SPIO-loaded micelles (Fig. 4D).

## The effect of SPIO on the Doxo release from micelle

We also investigated the in vitro release profile of Doxo from Doxo-SPIO-micelles and Doxo-micelles (Fig. 5). The release of Doxo from Doxo-SPIO-micelles showed a more sustained characteristics than that of Doxo-micelles. In addition, it showed that PH-sensitivity mediated Doxo release. In comparison, 25% drug release from SPIO-loaded micelles was slower than 25% of drug release from SPIO-free micelles in 48 hrs at pH 7.4.

## Effect of SPIO-clustering on MR sensitivity of of Doxo-SPIO-micelles

To help understand the MR properties, we measured the magnetization of Doxo-SPIO-loaded micelle using an alternating gradient magnetometer (AGM, Princeton Measurements) at room temperature and up to 0.4 T. (Fig. 6A). The values of magnetic moment at 0.4 T, where all the MRI measurements were conducted, reached the saturation value ( $M_{\text{sat}}$ ). The values of  $M_{\text{sat}}$  per unit metal mass were 78.6, 89.5

and 106.2 emu/g M for the micelle, made from 10:2.5:2, 10:5:2 and 10:10:2 ratio of components, respectively. The  $M_{\text{sat}}$  values are well correlated with those of  $r_2$ , consistent with the hypothesis that higher magnetization would result in larger field in homogeneities surrounding SPIO and more effective  $T_2$  relaxation of water molecules (Fig. 6B).

Fig. 6B shows that  $r_2$  values of Doxo-SPIO-micelles were further increased in PEG-PLA micelles where a cluster of SPIO was loaded. 7 nm SPIO loaded micelle showed the increased  $r_2$  values (221.3, 290.5, and 319.8  $\text{mM}^{-1} \text{s}^{-1}$ ), as the ratio of SPIO was increased (10:2.5:2, 10:5:2 and 10:10:2), respectively.

## In vitro cellular uptake behavior of Doxo-SPIO-micelles

The cellular uptake of each Doxo-SPIO-micelle was estimated by flow cytometry and confocal imaging analysis of cells. As shown in Fig. 7A and S2, the uptake decreased as the loading amount of SPIO increased. In the other hand, the MR sensitivity of cells after the uptake of Doxo-SPIO-micelles increased as the loading amount of SPIO increased (Fig. 7B).

## In vivo pharmacokinetics of Doxo-SPIO-micelles

As shown in Fig. 8, Doxo-SPIO-micelles showed a sustained blood concentration profile, compared to Doxo-micelles and free Doxo. The Doxo-SPIO-micelles had an AUC of  $3310.6 \pm 449.7 \mu\text{g}\cdot\text{min}\cdot\text{mL}^{-1}$  and a  $T_{1/2}$  of  $50.5 \pm 1.8$  min, while Doxo-micelles had an AUC of  $908.1 \pm 85.5 \mu\text{g}\cdot\text{min}\cdot\text{mL}^{-1}$ , and a  $T_{1/2}$  of  $12.4 \pm 0.6$  min (Table 1). In addition, quantification of Doxo content in kidneys, liver, lungs, spleen, muscle, and heart were collected and from mice euthanized after experiments. Fluorescence images in each sample was obtained (Fig. 9C and 9D) and statistical graph of fluorescence intensity was determined (Fig. 9A and 9B). High concentration of Doxo were accumulated in liver, lung and kidney after 12 h treatment.

Table 1

Pharmacokinetic parameters after intravenous injection of free Doxo, Doxo-micelles, and SPIO-Doxo-micelles against mice at a dose of  $2.5 \text{ mg Doxo}\cdot\text{kg}^{-1}$  ( $n=3$ , mean  $\pm$  stdev).

	Free Doxo	Doxo-micelles	Doxo-SPIO-micelles
AUC ( $\mu\text{g}\cdot\text{min}\cdot\text{mL}^{-1}$ )	$44.4 \pm 4.6$	$908 \pm 86$	$3310.6 \pm 449.7$
$t_{1/2}$ (min)	$2.1 \pm 0.6$	$12.4 \pm 0.6$	$50.5 \pm 1.8$
CL ( $\text{mL}\cdot\text{min}^{-1}\cdot\text{kg}^{-1}$ )	$56.2 \pm 10.9$	$2.7 \pm 0.2$	$0.76 \pm 0.1$
MRT (min)	$3.0 \pm 0.8$	$17.9 \pm 0.9$	$72.9 \pm 2.6$
$V_{\text{ss}}$ (mL)	$172.9 \pm 27.5$	$49.0 \pm 7.3$	$55.4 \pm 5.5$

## Discussion

In this work, SPIO-loading polymeric micelles and SPIO-free polymeric micelles were synthesized to confirm the effect of SPIO loading on hydrodynamic size and stability of micelle. Here, we observed the clustering of SPIO in the micelle core affected the size of micelle due to hydrophobic SPIO and micellization energy. The negative values of the micellization energy indicate that the micelle formation is spontaneous as it is a thermodynamically favorable process. In addition, SPIO induce stronger hydrophobic interaction, formed kinetically more stable micelles, and would maintain their structural integrity for longer time even below the CMC. According to the excellent stability of SPIO-loading micelles, effect of SPIO improved DLE on drug loading and release. Further study, DPP is exposed in viscous or glassy environment, excimer form of DPP significantly decreases, resulting in a lower value of  $I_e/I_m$  [27]. We consider this reflects the glass transition temperature ( $T_g$ ) of the PLA micelle core in aqueous solution. At the temperatures above the  $T_g$ , the micelle core becomes more fluidic, therefore facilitates the formation of excimer over monomer. This value (37.3°C) is consistent with the  $T_g$  value as determined by Kataoka and coworkers by the  $^1\text{H}$  NMR experiments [28]. This biphasic behavior was absent in SPIO-loaded micelles. In addition, the  $I_e/I_m$  values were much lower for SPIO-free micelles than SPIO-loaded micelles at all temperatures. More specifically at 37°C, the  $I_e/I_m$  value for SPIO-free micelles was 0.07 compared to 0.19 for SPIO-loaded micelles. These data suggest that incorporation of SPIO considerably increases the fluidity and flexibility in the micelle core, which may reflect the plasticizing effect of the unsaturated hydrocarbon chains of oleic acids from SPIO surface [29]. Together with the increase of the micelle core volume as the result of SPIO loading, these two factors may be the primary contributing factor for the dramatic increase in drug loading content and efficiency.

In addition, our study indicated that release of Doxo from SPION-micelles was sustained and PH-sensitive Doxo release, that is suggesting a stronger Doxo-micelle core interaction compared to the interaction in SPIO-free Doxo-micelles. However, both micelle formulations showed pH-sensitive release properties, which is beneficial for Doxo accumulation to the acidic tumor environment [15, 18, 30]. As we know, SPIO, that serve as an MRI candidate, affected the MR property, and the highest increase of  $r_2$  values was observed in 7nm SPIO loaded micelles (10:10:2) with the highest clustering tendency as shown in TEM images suggesting clustering enhanced the MR sensitivity. This also suggests polymeric micelle can be the most profit nano design to get highly sufficient MR sensitivity in vivo.

Generally, Surface chemistry of nanoparticles such as surface charge, targeting moiety and lipophilicity highly affects the cellular uptake of nanoparticles [31–33]. In this study, surface chemistry is not so proper to explain the observed different uptake efficiency, because all Doxo-SPIO-micelles have the same surface chemistry with PEG (5k) of corona layer.

Particle size also has been regarded as potential factor affecting cellular uptake. Desai et al proved PLGA microparticles with different size of 10  $\mu\text{m}$ , 1  $\mu\text{m}$  and 0.1  $\mu\text{m}$  showed clearly different cellular uptake efficiency [34]. The 0.1  $\mu\text{m}$  diameter particles had 2.5- and 6-folds higher uptake than 1 and 10  $\mu\text{m}$  diameters of microparticles, respectively. However, for the nanoparticles in range of 10 to 100 nm, the effect of different size on the cellular uptake remains poorly understood. Recently, Chithrani et al proved

50 nm of gold nanoparticles had a much higher uptake efficiency compared to the other size (e.g. 20 or 100 nm) of gold nanoparticles [35]. The other study also proved the 107 nm dextran crosslinked SPIO exhibited the highest uptake efficiency by T cells, compared to 33.4 and 52.5 nm of dextran crosslinked SPIO [36]. These observations imply the cellular uptake of nanoparticles (around 100 nm) is not always dependent on the size. For the polymeric micelles, the efficient way to control the micelle size by 10 to 20 nm units like inorganic nanoparticles is not fully established yet. Consequently, the size dependency on the cellular uptake of micelles is still unambiguous. In this study, the cellular uptake of Doxo-SPIO-micelles proved to be dependent on the amount of SPIO in micelle core as well as micelle size. Thus, we hypothesize that SPIO possibly change “the rigidity of micelles” that may affect trafficking process of micelle through cell membrane. For the proof of this hypothesis, the more intensive studies are required on this stage.

In vivo study, a sustained blood concentration and high intensity of Doxo on the kidney, lung, and liver were observed at Doxo-SPIO-micelles, whereas Doxo-micelles and Doxo showed more rapid clearances evidently. Doxo-SPIO-micelles, as the candidate for drug delivery, is a potential therapeutic strategy for cancer eradication.

## Conclusion

In summary, we have reported the effects of co-encapsulation of SPIO with Doxo into polymeric micelles on the physical and biological properties of the micelles in vitro and in vivo. Clustering of SPIO inside Doxo-micelles significantly increased drug loading content and drug loading efficiency. SPIO improved the thermodynamic stability of the micelles by decreasing their CMC and the kinetic stability. Doxo-SPIO-micelles also showed prolonged circulation half-life in animals, and superb in vivo stability as shown by TEM and MRI. The improved properties of the micelles will allow for the development of integrated nanomedicine with high drug loading contents, prolong the blood half-life, and excellent in vitro and in vivo stabilities for future therapeutic and diagnostic applications.

## Abbreviations

Superparamagnetic iron oxide nanoparticles (SPIO); Doxorubicin (Doxo); poly(ethylene glycol)-co-poly(D,L-lactide) (PEG-PLA); Area Under Curve (AUC); magnetic resonance imaging (MRI); SPIO and Doxo loaded polymeric micelles (Doxo-SPIO-micelles); drug loading content (DLC); Critical micelle concentration (CMC); drug loading efficiency (DLE); transmission electron microscopy (TEM); 1,3-(1,1'-dipyrenyl)-propane (DPP) emission intensity of DPP excimer at 478 nm ( $I_e$ ); emission intensity of DPP monomer at 377 nm ( $I_m$ )

## Declarations

## Acknowledgements

This work was supported by the Basic Science Research Program and the Bio & Medical Technology Development Program of the National Research Foundation (NRF) funded by the Korean government (MOE and MSIT) (2020R1I1A1A01073559, 2020R1A2B5B02002377, 2018R1A6A1A03025523, and 2019M3E5D1A02069623).

### **Authors' contributions**

Su-Geun Yang, Yixin Jiang and Junghan Lee performed experiments in vitro and in vivo studies.

Hye-Min Park, Kyung-Ju Shin revised the manuscript and prepared the figures.

Su-Geun Yang conceived and designed the study.

And all authors approved the final version of the manuscript.

### **Funding**

This work was supported by the Basic Science Research Program and the Bio & Medical Technology Development Program of the National Research Foundation (NRF) funded by the Korean government (MOE and MSIT) (2020R1A2B5B02002377, 2018R1A6A1A03025523, and 2019M3E5D1A02069623).

### **Availability of data and materials**

The authors confirm that the data supporting the findings of this study are available within the article [and/or] its supplementary materials.

### **Ethics approval and consent to participate**

Not applicable.

### **Consent for publication**

Not applicable.

### **Competing interests**

The authors declare no conflict of interest.

## **References**

1. Khemtong C, Kessinger CW, Gao JM. Polymeric nanomedicine for cancer MR imaging and drug delivery. *Chemical Communications*. 2009(24):3497-510. <https://doi.org/10.1039/b821865j>.
2. Kim J, Piao Y, Hyeon T. Multifunctional nanostructured materials for multimodal imaging, and simultaneous imaging and therapy. *Chemical Society Reviews*. 2009;38(2):372-90. <https://doi.org/10.1039/b709883a>.

3. Riehemann K, Schneider SW, Luger TA, Godin B, Ferrari M, Fuchs H. Nanomedicine-Challenge and Perspectives. *Angewandte Chemie-International Edition*. 2009;48(5):872-97.  
<https://doi.org/10.1002/anie.200802585>.
4. Gao JH, Gu HW, Xu B. Multifunctional Magnetic Nanoparticles: Design, Synthesis, and Biomedical Applications. *Accounts of Chemical Research*. 2009;42(8):1097-107.  
<https://doi.org/10.1021/ar9000026>.
5. Lee DE, Koo H, Sun IC, Ryu JH, Kim K, Kwon IC. Multifunctional nanoparticles for multimodal imaging and theragnosis. *Chemical Society Reviews*. 2012;41(7):2656-72.  
<https://doi.org/10.1039/c2cs15261d>.
6. Li YN, Zhang H. Fe<sub>3</sub>O<sub>4</sub>-based nanotheranostics for magnetic resonance imaging-synergized multifunctional cancer management. *Nanomedicine*. 2019;14(11):1493-512.  
<https://doi.org/10.2217/nnm-2018-0346>.
7. Chen HP, Chen MH, Tung FI, Liu TY. A novel micelle-forming material used for preparing a theranostic vehicle exhibiting enhanced in vivo therapeutic efficacy. *J Med Chem*. 2015;58(9):3704-19.  
<https://doi.org/10.1021/jm501996y>.
8. Lin W, Zhang X, Qian L, Yao N, Pan Y, Zhang L. Doxorubicin-Loaded Unimolecular Micelle-Stabilized Gold Nanoparticles as a Theranostic Nanoplatfrom for Tumor-Targeted Chemotherapy and Computed Tomography Imaging. *Biomacromolecules*. 2017;18(12):3869-80.  
<https://doi.org/10.1021/acs.biomac.7b00810>.
9. Kang S, Baskaran R, Ozlu B, et al. T<sub>1</sub>-Positive Mn(2+)-Doped Multi-Stimuli Responsive poly(L-DOPA) Nanoparticles for Photothermal and Photodynamic Combination Cancer Therapy. *Biomedicines*. 2020;8(10). <https://doi.org/10.3390/biomedicines8100417>.
10. McCarthy JR, Weissleder R. Multifunctional magnetic nanoparticles for targeted imaging and therapy. *Advanced Drug Delivery Reviews*. 2008;60(11):1241-51.  
<https://doi.org/10.1016/j.addr.2008.03.014>.
11. Wu K, Su DQ, Liu JM, Saha R, Wang JP. Magnetic nanoparticles in nanomedicine: a review of recent advances. *Nanotechnology*. 2019;30(50). <https://doi.org/10.1088/1361-6528/ab4241>.
12. Zhi DF, Yang T, Yang J, Fu S, Zhang SB. Targeting strategies for superparamagnetic iron oxide nanoparticles in cancer therapy. *Acta Biomaterialia*. 2020;102:13-34.  
<https://doi.org/10.1016/j.actbio.2019.11.027>.
13. Yew YP, Shameli K, Miyake M, et al. Green biosynthesis of superparamagnetic magnetite Fe<sub>3</sub>O<sub>4</sub> nanoparticles and biomedical applications in targeted anticancer drug delivery system: A review. *Arabian Journal of Chemistry*. 2020;13(1):2287-308. <https://doi.org/10.1016/j.arabjc.2018.04.013>.
14. Pope-Harman A, Cheng MMC, Robertson F, Sakamoto J, Ferrari M. Biomedical nanotechnology for cancer. *Medical Clinics of North America*. 2007;91(5):899-+.  
<https://doi.org/10.1016/j.mcna.2007.05.008>.
15. Nasongkla N, Bey E, Ren JM, et al. Multifunctional polymeric micelles as cancer-targeted, MRI-ultrasensitive drug delivery systems. *Nano Letters*. 2006;6(11):2427-30.

<https://doi.org/10.1021/nl061412u>.

16. Yang J, Lu W, Xiao J, et al. A positron emission tomography image-guidable unimolecular micelle nanoplatform for cancer theranostic applications. *Acta Biomater.* 2018;79:306-16. <https://doi.org/10.1016/j.actbio.2018.08.036>.
17. Ai H, Flask C, Weinberg B, et al. Magnetite-loaded polymeric micelles as ultrasensitive magnetic-resonance probes. *Advanced Materials.* 2005;17(16):1949-52.
18. Nasongkla N, Bey E, Ren J, et al. Multifunctional polymeric micelles as cancer-targeted, MRI-ultrasensitive drug delivery systems. *Nano Lett.* 2006;6(11):2427-30.
19. Berret JF, Schonbeck N, Gazeau F, et al. Controlled clustering of superparamagnetic nanoparticles using block copolymers: design of new contrast agents for magnetic resonance imaging. *J Am Chem Soc.* 2006;128(5):1755-61.
20. Lu CY, Ji JS, Zhu XL, et al. T2-Weighted Magnetic Resonance Imaging of Hepatic Tumor Guided by SPIO-Loaded Nanostructured Lipid Carriers and Ferritin Reporter Genes. *Acs Applied Materials & Interfaces.* 2017;9(41):35548-61. <https://doi.org/10.1021/acsami.7b09879>.
21. Kitagawa T, Kosuge H, Uchida M, et al. RGD targeting of human ferritin iron oxide nanoparticles enhances in vivo MRI of vascular inflammation and angiogenesis in experimental carotid disease and abdominal aortic aneurysm. *Journal of Magnetic Resonance Imaging.* 2017;45(4):1144-53. <https://doi.org/10.1002/jmri.25459>.
22. Berret JF, Schonbeck N, Gazeau F, et al. Controlled clustering of superparamagnetic nanoparticles using block copolymers: Design of new contrast agents for magnetic resonance imaging. *Journal of the American Chemical Society.* 2006;128(5):1755-61. <https://doi.org/10.1021/ja0562999>.
23. Sun S, Zeng H, Robinson DB, et al. Monodisperse MFe<sub>2</sub>O<sub>4</sub> (M = Fe, Co, Mn) nanoparticles. *J Am Chem Soc.* 2004;126(1):273-9.
24. La SB, Okano T, Kataoka K. Preparation and characterization of the micelle-forming polymeric drug indomethacin-incorporated poly(ethylene oxide)-poly(beta-benzyl L-aspartate) block copolymer micelles. *Journal of Pharmaceutical Sciences.* 1996;85(1):85-90. <https://doi.org/10.1021/js950204r>.
25. Charrois GJ, Allen TM. Drug release rate influences the pharmacokinetics, biodistribution, therapeutic activity, and toxicity of pegylated liposomal doxorubicin formulations in murine breast cancer. *Biochim Biophys Acta.* 2004;1663(1-2):167-77.
26. Lang AD, Zhai J, Huang CH, et al. Relationship between structures and photocurrent generation properties in a series of hemicyanine congeners. *Journal of Physical Chemistry B.* 1998;102(8):1424-29. <https://doi.org/10.1021/jp972429r>.
27. Pozuelo J, Atvars TDZ, Bravo J, Baselga J. Host/guest simulation of fluorescent probes adsorbed into low-density polyethylene, 1 - Excimer formation of 1,3-Di(1-pyrenyl)propane. *Macromolecular Theory and Simulations.* 2001;10(9):808-15. [https://doi.org/10.1002/1521-3919\(20011101\)10:9<808::aid-mats808>3.0.co;2-i](https://doi.org/10.1002/1521-3919(20011101)10:9<808::aid-mats808>3.0.co;2-i).
28. Yamamoto Y, Yasugi K, Harada A, Nagasaki Y, Kataoka K. Temperature-related change in the properties relevant to drug delivery of poly(ethylene glycol)-poly(D,L-lactide) block copolymer

- micelles in aqueous milieu. *J Control Release*. 2002;82(2-3):359-71. [https://doi.org/10.1016/s0168-3659\(02\)00147-5](https://doi.org/10.1016/s0168-3659(02)00147-5).
29. Cai S, Vijayan K, Cheng D, Lima EM, Discher DE. Micelles of different morphologies—advantages of worm-like filomicelles of PEO-PCL in paclitaxel delivery. *Pharm Res*. 2007;24(11):2099-109. <https://doi.org/10.1007/s11095-007-9335-z>.
  30. Hruby M, Konak C, Ulbrich K. Polymeric micellar pH-sensitive drug delivery system for doxorubicin. *Journal of Controlled Release*. 2005;103(1):137-48. <https://doi.org/10.1016/j.jconrel.2004.11.017>.
  31. Hayes ME, Drummond DC, Hong K, et al. Increased target specificity of anti-HER2 genospheres by modification of surface charge and degree of PEGylation. *Mol Pharm*. 2006;3(6):726-36.
  32. Chung TH, Wu SH, Yao M, et al. The effect of surface charge on the uptake and biological function of mesoporous silica nanoparticles in 3T3-L1 cells and human mesenchymal stem cells. *Biomaterials*. 2007;28(19):2959-66.
  33. Augustine R, Hasan A, Primavera R, Wilson RJ, Thakor AS, Kevadiya BD. Cellular uptake and retention of nanoparticles: Insights on particle properties and interaction with cellular components. *Materials Today Communications*. 2020;25:101692. <https://doi.org/https://doi.org/10.1016/j.mtcomm.2020.101692>.
  34. Desai MP, Labhasetwar V, Walter E, Levy RJ, Amidon GL. The mechanism of uptake of biodegradable microparticles in Caco-2 cells is size dependent. *Pharm Res*. 1997;14(11):1568-73.
  35. Chithrani BD, Ghazani AA, Chan WC. Determining the size and shape dependence of gold nanoparticle uptake into mammalian cells. *Nano Lett*. 2006;6(4):662-8.
  36. Thorek DL, Tsourkas A. Size, charge and concentration dependent uptake of iron oxide particles by non-phagocytic cells. *Biomaterials*. 2008;29(26):3583-90.

## Figures

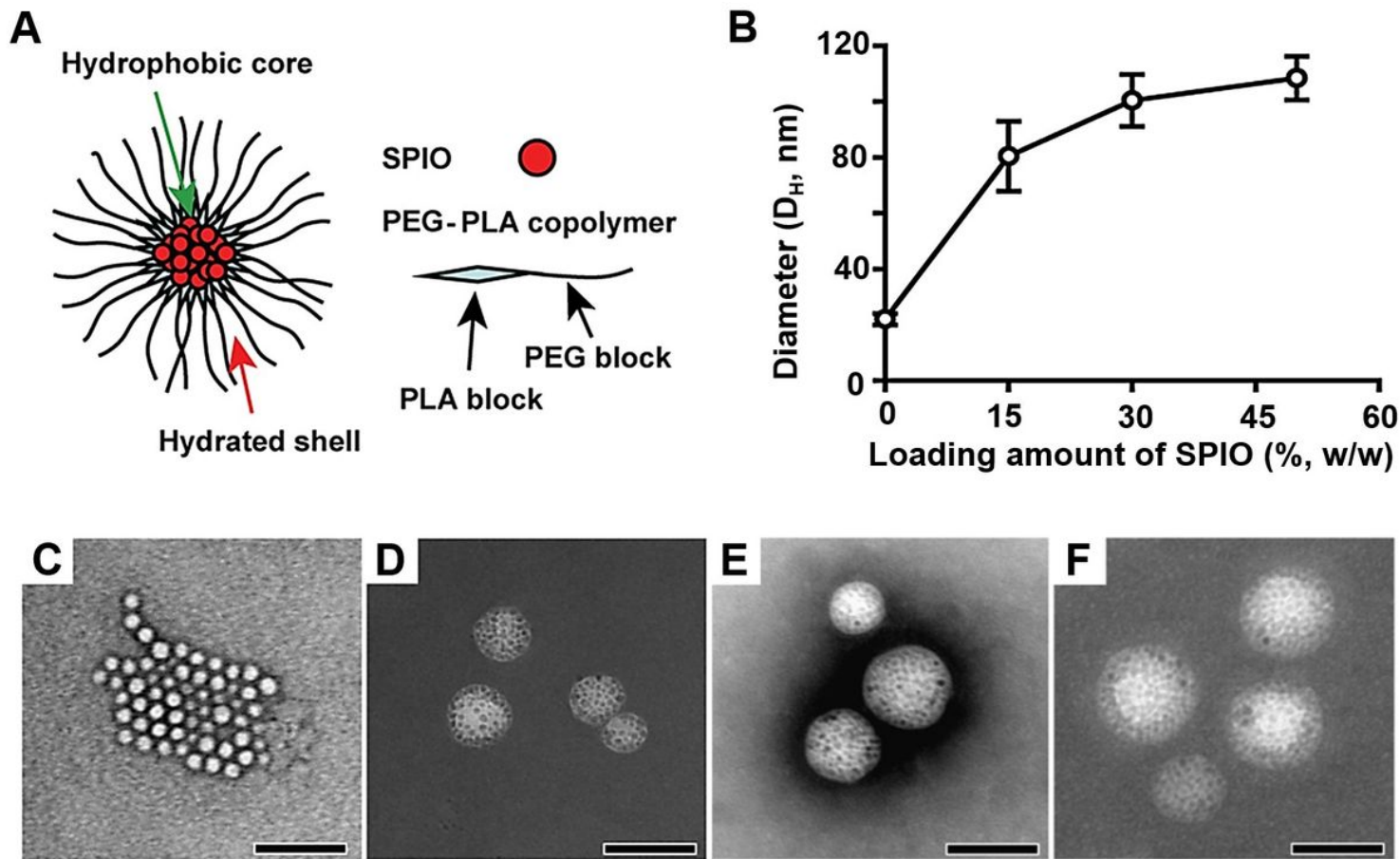


Figure 1

Effect of SPIO-clustering and loading on structure of PEG-PLA polymeric micelles. A) Structure of SPIO-loaded PEG-PLA micelles. (B) Hydrodynamic diameter of PEG-PLA polymeric micelles with 0, 15, 30, and 50% SPIO loading contents of SPIO. (C-F) TEM images of the micelles with 0, 15, 30, and 50% SPIO loading contents, Scale bar = 100 nm.

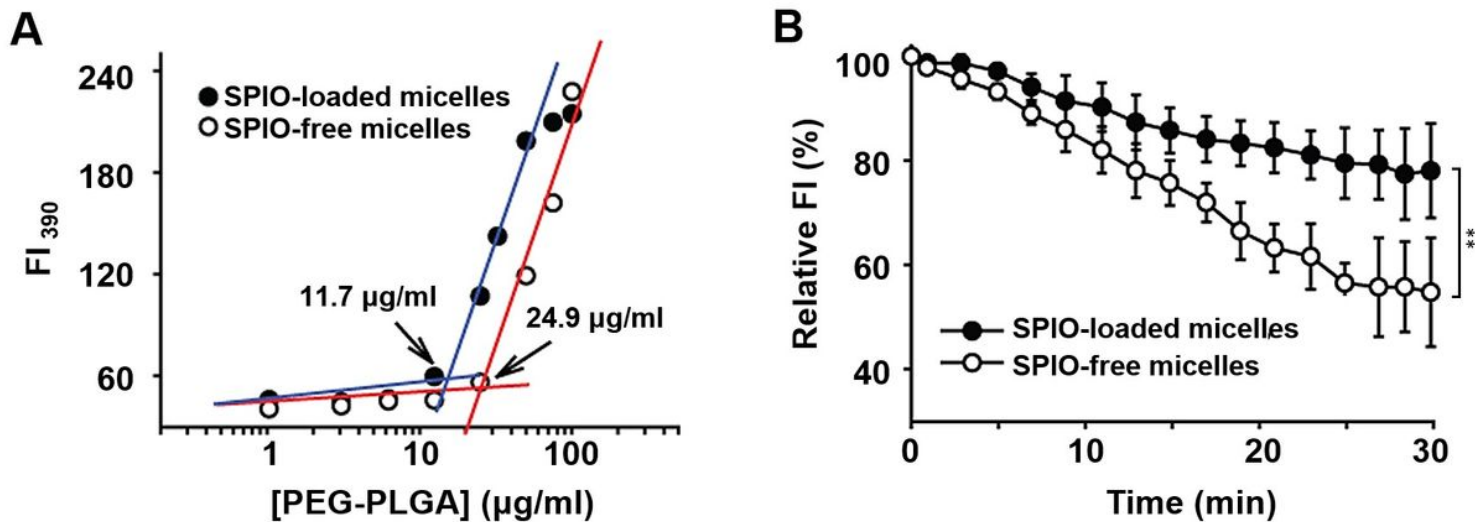
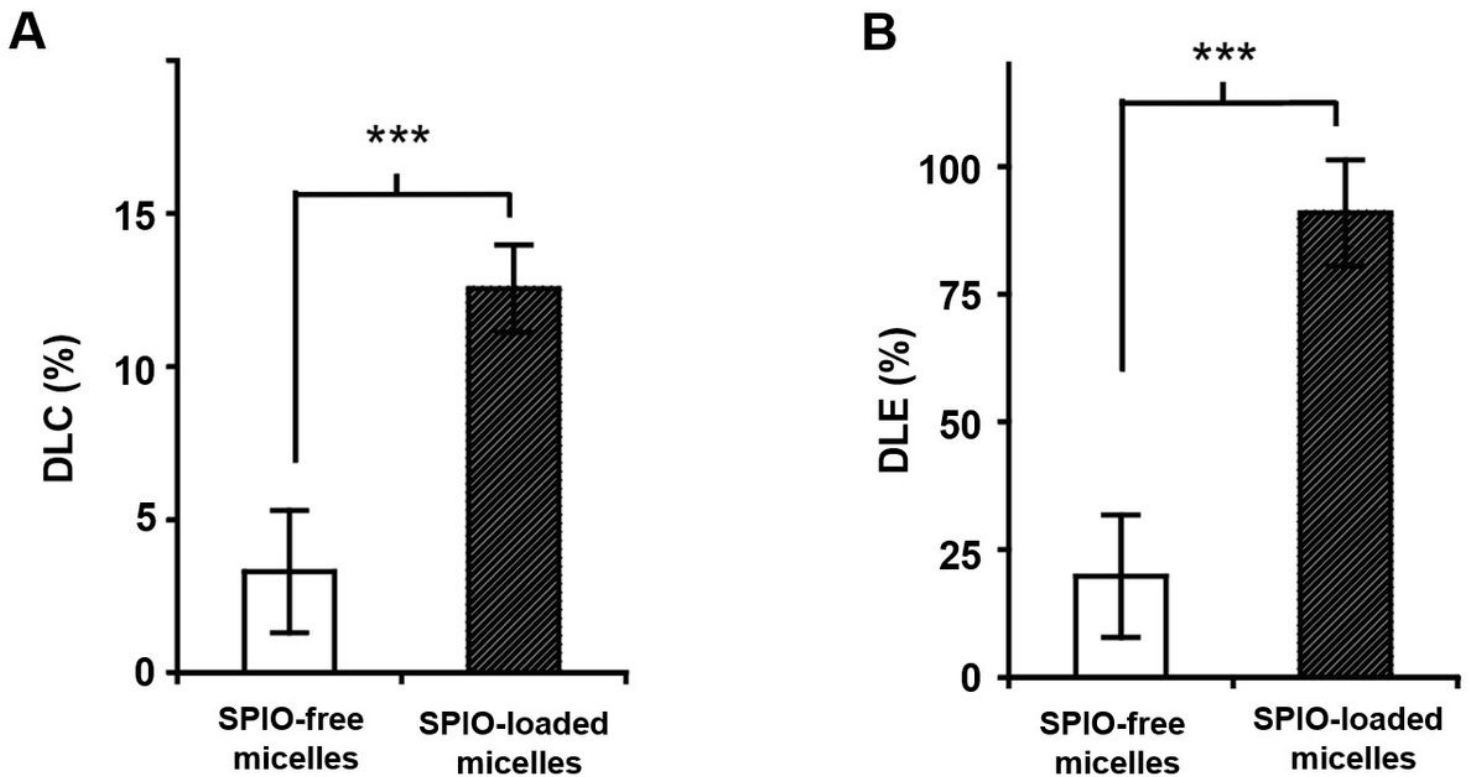


Figure 2

Effect of SPIO-clustering on thermodynamic stability of PEG-PLA polymeric micelles. (A) Effect of SPIO clustering on CMC of PEG-PLA (5k-5k) polymeric micelles. CMC was determined from fluorescence intensities of pyrene ( $\lambda_{em} = 390 \text{ nm}$ ,  $\lambda_{ex} = 333 \text{ nm}$ ) at different PEG-PLA concentrations. (B) Dissociation of SPIO-free micelles and SPIO-loaded micelles at the concentration of lower CMC ( $8 \mu\text{g}\cdot\text{mL}^{-1}$ ) at  $37^\circ\text{C}$ . Data are expressed as mean $\pm$ stdev, \*\*  $p < 0.05$ .



**Figure 3**

Effect of SPIO-clustering on drug loading of PEG-PLA polymeric micelles. (A) Drug loading content (DLC, %) and (B) drug loading efficiency (DLE, %) of SPIO-free and SPIO-loaded micelles (15% SPIO loading). DLE (%) was calculated using the following equation:  $[\text{estimated Doxo loading}] / [\text{theoretical Doxo loading}] \times 100$ . (C) Doxo loading content (%) of SPIO-loaded PEG-PLA micelles with mixing ratio of PEG-PLA and SPIO. Data are expressed as mean $\pm$ stdev, \*\*\*  $p < 0.01$ , \*\*  $p < 0.05$ .

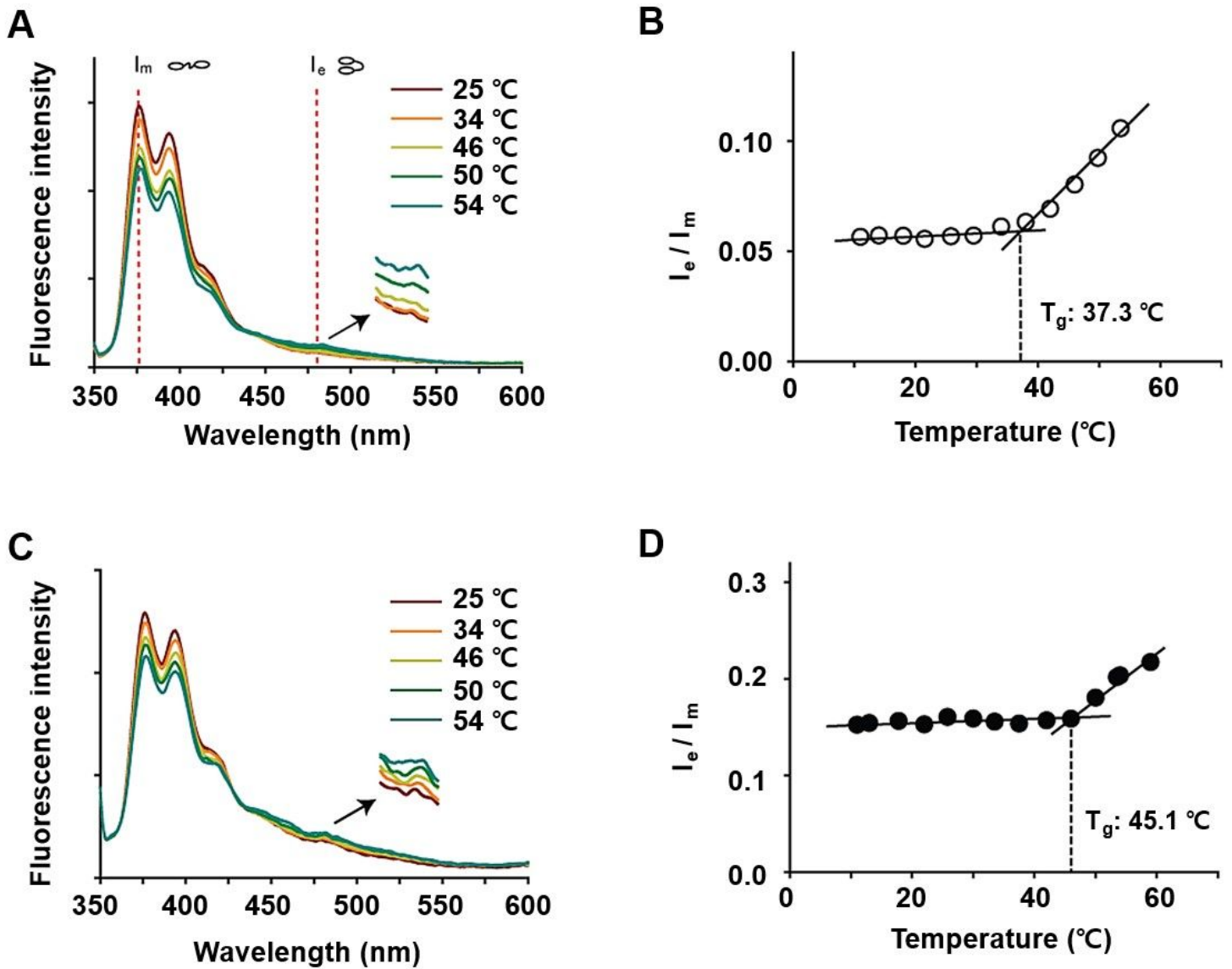
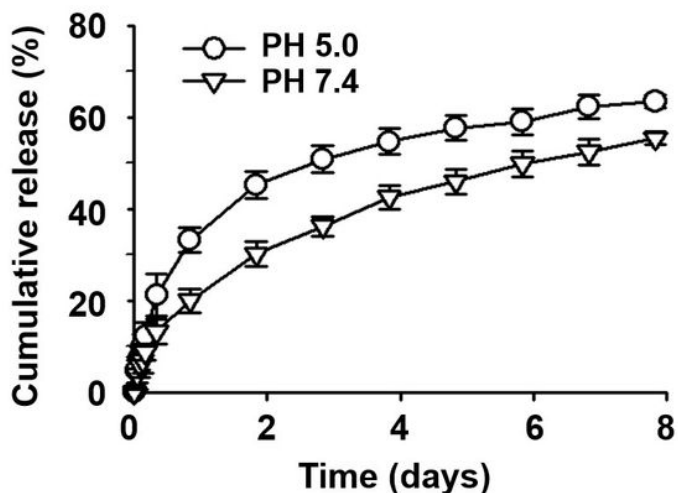


Figure 4

Effect of SPIO-clustering on thermodynamic stability of PEG-PLA polymeric micelles. Fluorescence emission spectra ( $\lambda_{ex} = 399\text{ nm}$ ) of 1,3-di(1,1'-pyrenyl)propane in SPIO-free micelles (A) and SPIO-loaded micelles (C). Fluorescence intensity ratio of excimer ( $\lambda_{em} = 478\text{ nm}$ ) to monomer ( $\lambda_{em} = 377\text{ nm}$ ) of 1,3-di(1,1'-pyrenyl)propane ( $I_e / I_m$ ) of SPIO-free micelles (B) and SPIO-micelles (D) at different temperatures.

### A Doxo-micelles



### B Doxo-SPIO-micelles

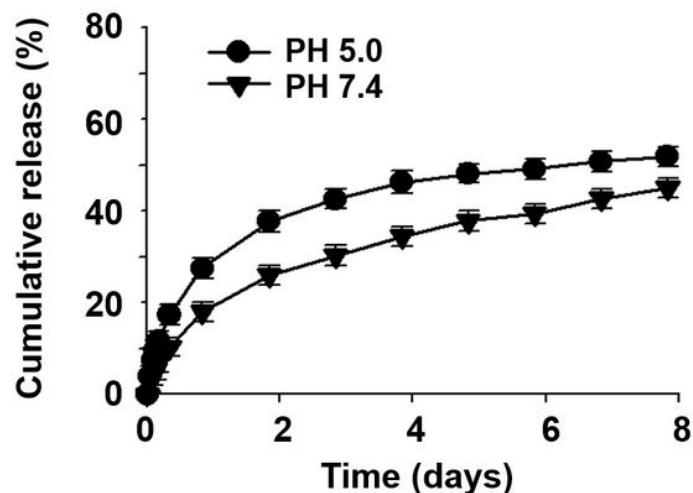
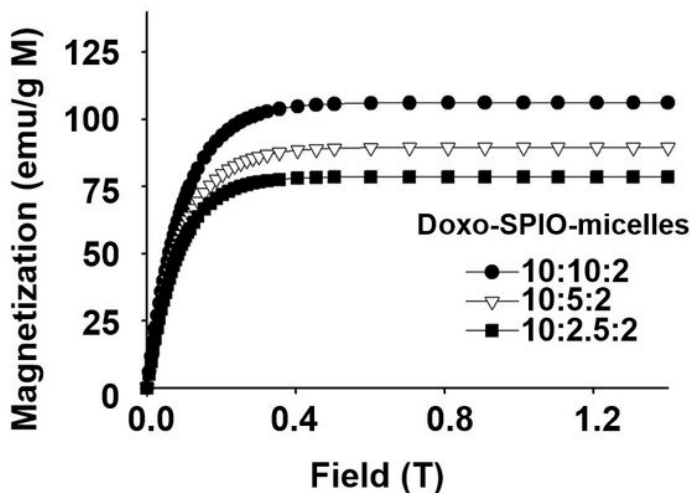


Figure 5

Effect of SPIO-clustering on drug release of PEG-PLA polymeric micelles. pH dependent release of Doxo from (A) SPIO free micelles (Doxo-micelles) and (B) SPIO loaded micelles (Doxo-SPIO-micelles).

### A



### B

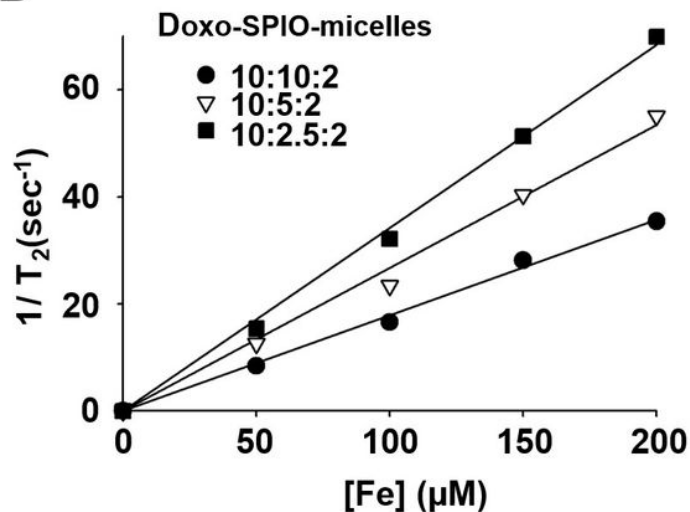
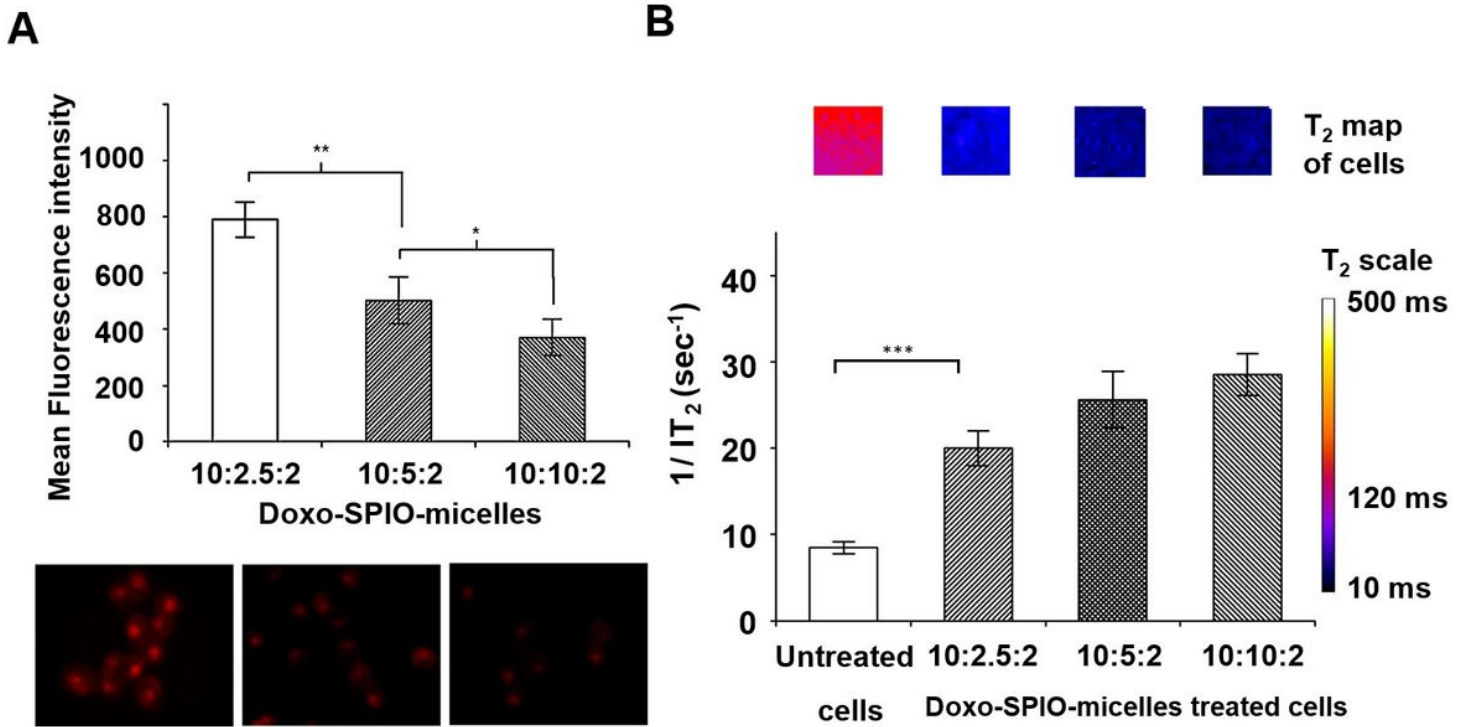


Figure 6

Effect of SPIO-clustering on MR sensitivity of PEG-PLA polymeric micelles. (A) Magnetization curves and (B) T<sub>2</sub> relaxation rates (1/T<sub>2</sub>, sec<sup>-1</sup>) of different formulations of Doxo-SPIO-micelles as a function of iron concentration. Doxo-SPIO-micelles were made from 10:2.5:2, 10:5:2 and 10:10:2 weight ratio of polymer:SPIO:Doxo.



**Figure 7**

Effect of SPIO-clustering on cellular uptake behaviors of PEG-PLA polymeric micelles. (A) Mean fluorescence intensity of H1299 cells by flow cytometry (up). Fluorescence laser scanning microscopy of H1299 cells after 2 hrs of incubation (down). Doxo fluorescent images were acquired at  $\lambda_{ex} = 485$  nm,  $\lambda_{em} = 595$  nm. (B) T<sub>2</sub> relaxation rates ( $1/T_2$ , sec<sup>-1</sup>) of the collected H2009 cells after treatment with Doxo-SPIO-micelles. The inset shows T<sub>2</sub> maps of cell samples. Data are expressed as mean $\pm$ stdev, \*\*  $p < 0.05$ , \*  $p < 0.1$ .

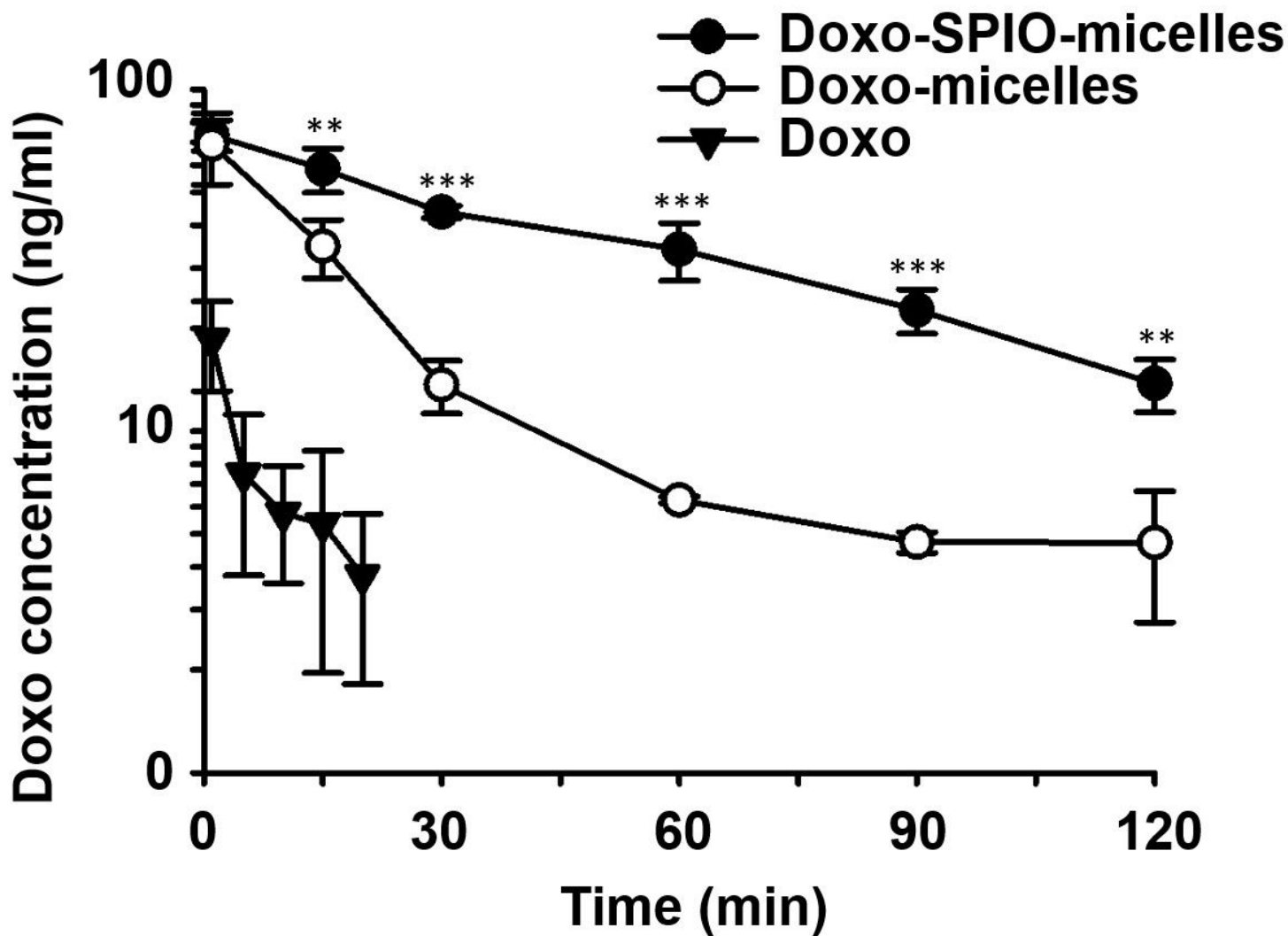
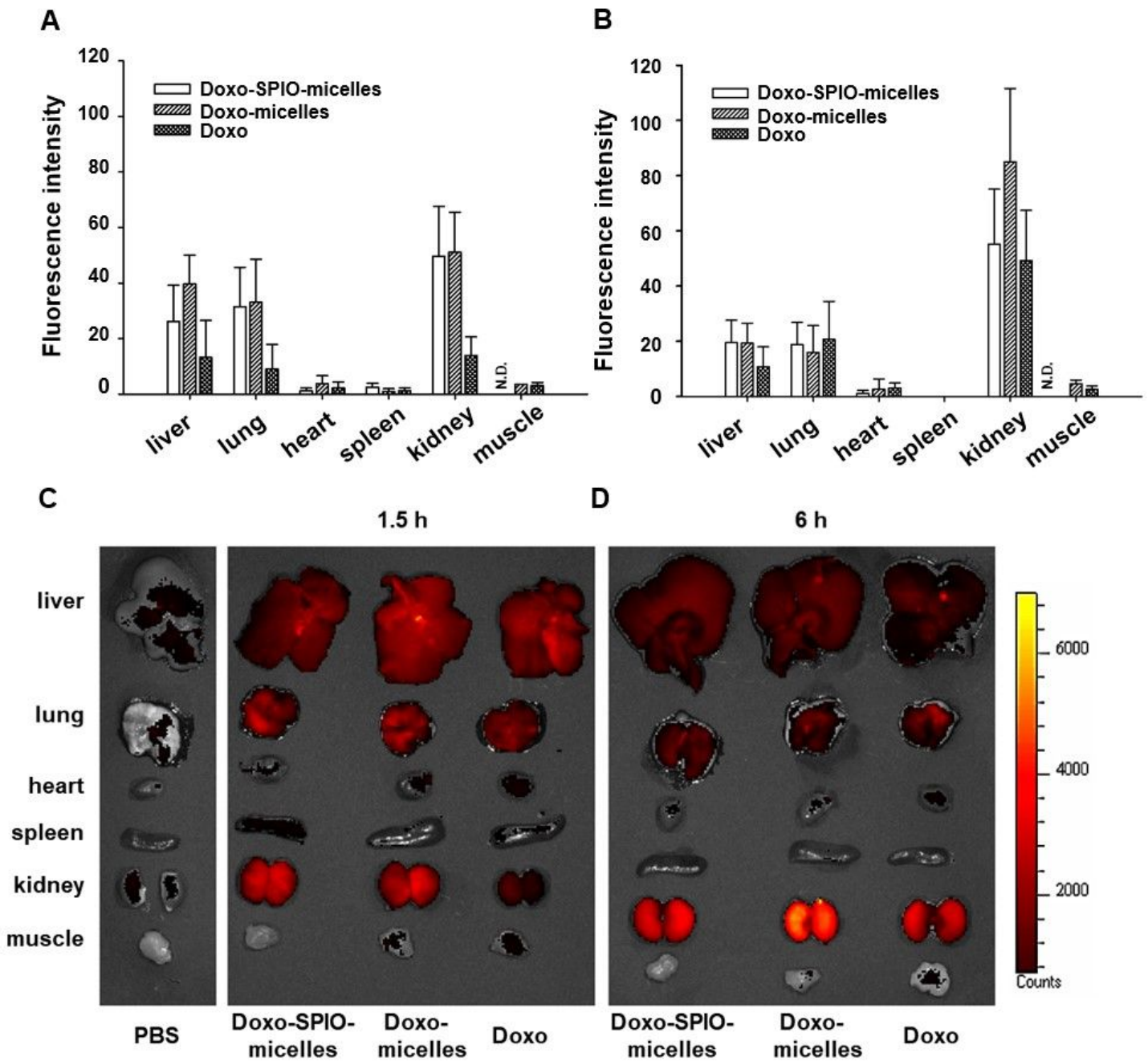


Figure 8

Effect of SPIO-clustering on pharmacokinetics of PEG-PLA polymeric micelles. Plasma concentration of Doxo was observed after i.v. injection of Doxo-SPIO-micelles, Doxo-micelles and free-Doxo at a 2.5 mg/kg Doxo dose. Statistical analysis of data was performed between Doxo-SPIO-micelles, Doxo-micelles (n=5, data are expressed as mean±stdev, \*p<0.1, \*\*p<0.05, \*\*\*p<0.01).



**Figure 9**

Effect of SPIO-clustering on organ distribution of PEG-PLA polymeric micelles. Fluorescence of each organ was observed after i.v. injection of Doxo-SPIO-micelles, Doxo-micelles and free-Doxo at a 2.5 mg/kg Doxo dose. (A and B) Mean fluorescence intensity of organs at 1.5 h and 6 h after the injection. (C and D) Photo-fluorescence images of organs at 1.5 h and 6 h after the injection.

## Supplementary Files

This is a list of supplementary files associated with this preprint. Click to download.

- 2021102.docx